

Northumbria Research Link

Citation: Ma, Tao, Yuan, Jinhui, Sun, Lei, Li, Feng, Kang, Zhe, Yan, Binbin, Sang, Xinzhu, Wang, Kuiru, Wu, Qiang, Liu, Heng, Gao, Jinhui and Yu, Chongxiu (2017) Highly Sensitive Biochemical Sensor Based on Two-Layer Dielectric Loaded Plasmonic Microring Resonator. *Plasmonics*, 12 (5). pp. 1417-1424. ISSN 1557-1955

Published by: Springer

URL: <https://doi.org/10.1007/s11468-016-0401-4> <<https://doi.org/10.1007/s11468-016-0401-4>>

This version was downloaded from Northumbria Research Link:
<http://nrl.northumbria.ac.uk/id/eprint/32251/>

Northumbria University has developed Northumbria Research Link (NRL) to enable users to access the University's research output. Copyright © and moral rights for items on NRL are retained by the individual author(s) and/or other copyright owners. Single copies of full items can be reproduced, displayed or performed, and given to third parties in any format or medium for personal research or study, educational, or not-for-profit purposes without prior permission or charge, provided the authors, title and full bibliographic details are given, as well as a hyperlink and/or URL to the original metadata page. The content must not be changed in any way. Full items must not be sold commercially in any format or medium without formal permission of the copyright holder. The full policy is available online: <http://nrl.northumbria.ac.uk/policies.html>

This document may differ from the final, published version of the research and has been made available online in accordance with publisher policies. To read and/or cite from the published version of the research, please visit the publisher's website (a subscription may be required.)

Highly sensitive biochemical sensor based on two-layers dielectric loaded plasmonic microring resonator

Tao Ma^{1,2}, Jinhui Yuan^{1,3*}, Lei Sun¹, Feng Li³, Zhe Kang³, Binbin Yan¹, Xinzhu Sang¹, Kuiru Wang¹, Oiang Wu^{4,5}, Heng Liu², Jinhui Gao², and Chongxiu Yu¹

¹State Key Laboratory of Information Photonics and Optical Communications, Beijing University of Posts and Telecommunications (BUPT), Beijing 100876, China

²College of Electronic and Electrical Engineering, Henan Normal University, Xinxiang 453007, China

³Photonics Research Center, Department of Electronic and Information Engineering, The Hong Kong Polytechnic University, Hung Hom, Kowloon, Hong Kong, China

⁴Photonics Research Center, School of Electronic and Communications Engineering, Dublin Institute of Technology, Kevin Street, Dublin 8, Ireland

⁵Department of Physics and Electrical Engineering, Northumbria University, Newcastle Upon Tyne, NE1 8ST, United Kingdom

*E-mail: yuanjinhui81@163.com

Abstract In this paper, we propose and design a highly sensitive optical biochemical sensor based on two-layers dielectric loaded surface plasmon polariton waveguide (TDLSPPW)-based microring resonator (MRR). By optimizing the structure parameters, the propagation length of the proposed waveguide is $\sim 126 \mu\text{m}$, which is about 3 times of that of the polymer dielectric loaded surface plasmon polariton waveguide (DLSPPW) reported. It is demonstrated that the TDLSPPW-based MRR is operated at the under-coupling state, along with the quality factor (Q) of 541.2 and extinction ratio (ER) of 12.2 dB. Moreover, the Q and ER are much more sensitive to the structure parameters of the waveguide, including the waveguide width w , total thickness t , and coupling gap W_{gap} , compared to the low refractive index (RI) layer thickness t_2 . The simulation results on the biochemical RI sensing show that the sensitivities of 408.7 and 276.4 nm/RIU for glucose concentration in urine and chemical gases can be achieved, respectively. It is believed that the

proposed sensor has potential applications in photonic-integrated biochemical sensing.

Keywords Surface plasmon resonant. Optical waveguide. Dielectric-loaded plasmonic waveguide

1. Introduction

Surface plasmon polaritons (SPPs) are transverse magnetic (TM) surface modes, which are generated at the interface between metal and dielectric due to the coupling between the photons and free electron density fluctuation on the metal surface. The SPPs modes show several fascinating features such as the ability to be guided beyond the diffraction limit, a strong enhancement of the local fields, and highly sensitive to interaction with the surrounding environment [1]. In the last decade, various SPPs waveguides have been proposed and designed. Among them, dielectric loaded surface plasmon polariton waveguides (DLSPPWs) [2, 3] have several unique advantages, including

technological simplification, compatible with different dielectrics, and easy to fabrication by using large-scale UV lithography. In addition, because of the strong guiding property, the DLSPPWs allow for bend elements with negligible bend loss. Thus, it can be applied to dense integrated photonic circuits. Until now, the DLSPPWs have been extensively investigated to realize the directional couplers [4], polarization converter [5], Mach-Zehnder interferometer [6, 7], electro-optic switch [8], thermo-optic modulation components [9], and refractive index (RI) sensor [10].

The optical devices based on microring resonators (MRRs) have attracted great interest, especially for highly sensitive sensing. Because the performance of micrometer-scale ring resonator highly depends on the bending loss, the strong mode confinement and low propagation loss should be satisfied simultaneously. The SPPs waveguide is a good candidate as it supports SPPs modes, which is propagated around the sharp bends with subwavelength confinement [11]. The two-layers dielectric loaded surface plasmon polariton waveguide (TDLSPPW)-based MRRs have also been widely studied [12-14]. Unfortunately, for sensing application, the TDLSPPW-based MRRs have a key disadvantage due to its high propagation loss. When the RIs of analytes detected are close to that of the DLSPPs waveguides, the optical field confinement evidently decreases, and the propagation length sharply reduces. So it is necessary to increase the propagation length for high performance of the proposed TDLSPPW-based MRR. The influence of propagation losses can be reduced by integration of short DLSPPWs with long dielectric waveguides [15]. A design of a very thin metallic film in a dielectric core is used to increase the propagation length [16]. Some hybrid SPPs waveguides are also demonstrated to increase the

propagation length [17, 18]. Recently, a TDLSPPW has preliminarily been proposed to increase the propagation length [19]. However, to the best of our knowledge, there are no relevant reports on the TDLSPPW-based MRRs for sensing application.

In this paper, we propose and design a biochemical sensor made of the $\text{MoO}_3\text{-MgF}_2$ TDLSPPW-based MRR. The propagation properties of the TDLSPPW are investigated by boundary mode analysis of the 3D finite element method (3D-FEM). The dependences of effective index n_{eff} , propagation length L_{prop} , and waveguide sensitivity S_{wg} on the structure parameters of the TDLSPPW are studied. Then, the frequency domain analysis is used to show the transmission characteristic and the sensing performance of the proposed TDLSPPW-based MRR. Quality factor (Q) and extinction ratio (ER) are also investigated. The effects of the waveguide shape deviations on the characteristics of the TDLSPPW-based MRR are also discussed. Finally, the sensing sensitivity (S) and detection limit (DL) of the TDLSPPW-based MRR based biochemical sensor for glucose concentration in urine and chemical gases are demonstrated.

2. TDLSPPW-based MRR structure

Figure 1 shows the structure of the proposed TDLSPPW-based MRR. Both the bus and ring waveguide are made of two layers dielectric with different RIs deposited on a 70 nm thick gold film, as shown in Fig. 2(a). Specifically, for wavelengths from 1500 to 1600 nm, the thickness of 70 nm is adequate for the exponentially decaying tail of the fundamental SPPs mode in metallic film [13]. The single-mode propagation of the DLSPP ridge waveguide can be realized for the thickness smaller than 630 nm and width below 655 nm [3]. In order to investigate the single-mode condition in the wavelength range from 1500 to

1600 nm, the width of the ridge waveguide w is chosen as 500 nm. The cross-section profile of the TDLSPPW is shown in Fig. 2(a). The two different RI dielectric layers of the TDLSPPW are MoO_3 and MgF_2 , respectively. The upper layer is MoO_3 with high RI of n_1 and a thickness t_1 , and the low-index part has a refractive index n_2 (MgF_2) and a thickness t_2 . The total thickness t of the TDLSPPW is also labeled in Fig. 2(a). The t and t_2 are the parameters used for the boundary mode analysis in section 3. The refractive index of gold, n_3 , is obtained from Ref 20. The microring radius R is chosen as $5 \mu\text{m}$ because the bending loss of the SPPs waveguide is reduced to 1 dB when the radius R is $5 \mu\text{m}$ [21]. The gap W_{gap} between the bus waveguide and the microring is also chosen as a parameter for the TDLSPPW-based MRR in the following simulation.

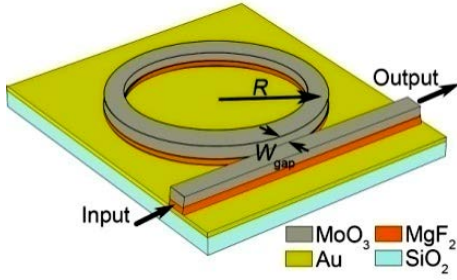


Fig. 1. Schematic of a TDLSPPW-based MRR.

The FEM is widely used to simulate the electromagnetic behavior in photonic devices [22] due to its accurate and fast simulation on the light interaction with the nanostructure [23]. The propagation properties of the TDLSPPWs can be investigated by boundary mode analysis of the 3D FEM simulation, which is also used to simulate the guided-modes of the input and output ports in the TDLSPWs waveguide. Subsequently, the frequency domain analysis of 3D FEM is employed to simulate the performance of the TDLSPWs MRR. The transmission response can be calculated by using S_{21}

$$S_{21} \text{ (dB)} = 10 \lg(P_o/P_i) \quad (1)$$

where P_i and P_o are the powers at the input and

output port, respectively.

The TDLSPPW-based MRR can be fabricated [19]. The gold film is coated on SiO_2 insulator layer by an electron gun evaporator. After coating the gold film, the MRR patterns are defined by electron beam exposure to a 700 nm thick polymethylmethacrylate (PMMA) layer which spin coating on the substrate. The MgF_2 layer ($n_2 = 1.35$) and MoO_3 layer ($n_1 = 2.06$) are deposited in sequence by a thermal evaporator. Then the TDLSPPW-based MRR can be formed after removing the PMMA by acetone.

3. Performance of the proposed device

A. Propagation characteristics

The TDLSPPW with top cladding of air ($n_c=1$) supports a hybrid plasmonic/photonic-like mode and a low-loss photonic-like mode, as shown in Fig. 2(b) and 2(c), respectively. The properties of these modes have been discussed [21]. The hybrid mode is a combination of a SPPs mode in low-RI layer and a guided-mode in high-RI layer. The electromagnetic energy of the hybrid mode is mainly distributed over the adjacent metal-dielectric interface inside low-index layer, which can effectively decrease the ohmic loss from the metal film and provide a better mode confinement. However, the photonic-like mode, which is similar to the guided-mode of rectangular dielectric waveguide, is not a SPPs mode.

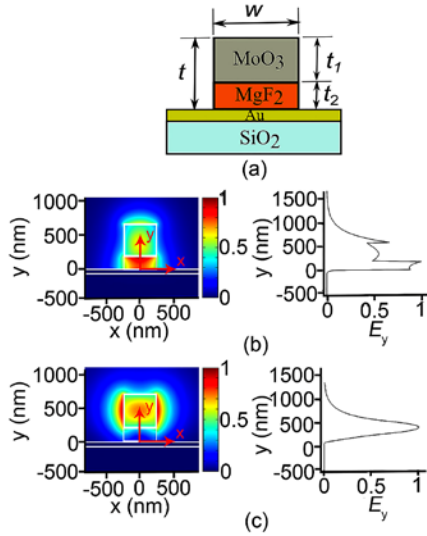


Fig. 2. (a) Cross-section profile of the proposed TDLSPW. (b) the hybrid mode, and (c) the photonic-like mode.

The guided-mode propagation in the TDLSPW greatly depends on its geometrical dimensions, especially the thickness [14]. Hence, the propagation properties of the TDLSPW at 1.55 μm are discussed with different t_2 and t . The propagation property of a plasmonic waveguide can be characterized through the effective index n_{eff} and propagation length L_{prop} . The n_{eff} of the TDLSPW can be calculated by boundary mode analysis of the 3D FEM simulation, and L_{prop} can be calculated as following [24]

$$L_{\text{prop}} = \frac{\lambda}{4\pi \times \text{Im}[n_{\text{eff}}]} \quad (2)$$

where λ is the wavelength in vacuum.

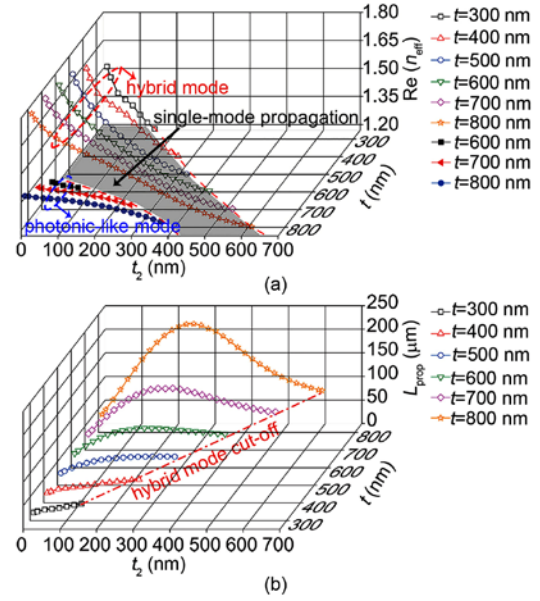


Fig. 3. (a) Real component of mode effective index of hybrid mode and photonic-like mode, and (b) L_{prop} of the hybrid mode with different h and t_2 at the wavelength of 1550nm.

The mode RI and L_{prop} of the TDLSPW as functions of t_2 and t are shown in Fig. 3(a) and 3(b), respectively. From Fig. 3(a) and 3(b), the real component of RI monotonically decreases with the increasing of t_2 for the same t , and increases with the increasing of t for the same t_2 for both the hybrid and photonic-like modes. It can be seen from Fig. 3(a) that only the hybrid mode can exist in the gray areas. L_{prop} monotonically increases with the increasing of t_2 when t is less than 600 nm. However, L_{prop} firstly increases to the maximum value, and then decreases when t is larger than 500 nm. In Fig. 3(b), all curves end at the points of the hybrid mode cut-off. The single-mode operation can be achieved for $t_2=270\sim510$ nm and $t=700$ nm. In order to achieve the longer L_{prop} , t and t_2 should be chosen as 700 and 280 nm, respectively. In this case, L_{prop} of the TDLSPW is $\sim 126 \mu\text{m}$, which is about 3 times of that of polymer DLSPPW ($\sim 42 \mu\text{m}$) [13].

For sensing application, the sensitivity S is a crucial parameter that defines the ability of a sensor to transduce an input signal to an output one.

Specifically, it can be defined as the amount of change in the optical parameters (e.g., wavelength, intensity, phase) induced by the surrounding analytes for optical sensing. For the resonant wavelength shift detection scheme, S is defined as the magnitude in shift of resonant wavelength ($\Delta\lambda_{\text{res}}$) versus the RI change (Δn_c) of the analytes detected which is induced by biological material and/or chemical concentration change. S of the RI sensor is given as following [25]

$$S = \frac{\Delta\lambda_{\text{res}}}{\Delta n_c} = \frac{\Delta\lambda_{\text{res}}}{\Delta n_{\text{eff}}} \cdot \frac{\Delta n_{\text{eff}}}{\Delta n_c} = S_{\text{dev}} S_{\text{wg}} \quad (3)$$

where Δn_{eff} is the change of n_{eff} , S_{dev} and S_{wg} are the device sensitivity and waveguide sensitivity, respectively. S_{dev} and S_{wg} can be given by [25]

$$S_{\text{dev}} = \frac{\Delta\lambda_{\text{res}}}{\Delta n_{\text{eff}}} = \frac{L}{m} \quad (4)$$

$$S_{\text{wg}} = \frac{\Delta n_{\text{eff}}}{\Delta n_c} \approx \left. \frac{dn_{\text{eff}}}{dn_c} \right|_{n_c} \quad (5)$$

where L and m stand for the circumference of the microring and resonance order, respectively. S_{dev} only depends on the device properties while S_{wg} depends on the waveguide structure. The design strategy is to optimize the S_{dev} and S_{wg} to improve S . At a fixed wavelength, the ratio L/m is a constant because the m varies linearly with L for the MRR detection scheme. Thus, S of the TDLSPs MRR sensor depends mainly on S_{wg} . The relationship between S_{wg} and n_c and t_2 is shown in Fig. 4(a). S_{wg} increases with the increasing of n_c and t_2 . L_{prop} of the TDLSPs waveguide as a function of n_c is also shown in Fig. 4(b). With the increase of n_c , L_{prop} firstly increases to the maximum value, and then decreases. Thus, $t=700$ nm and $t_2=280$ nm are reasonable for the propagation more than $90 \mu\text{m}$. S_{wg} varies from 0.31 to 0.69 as n_c is changed from 1 to 1.6.

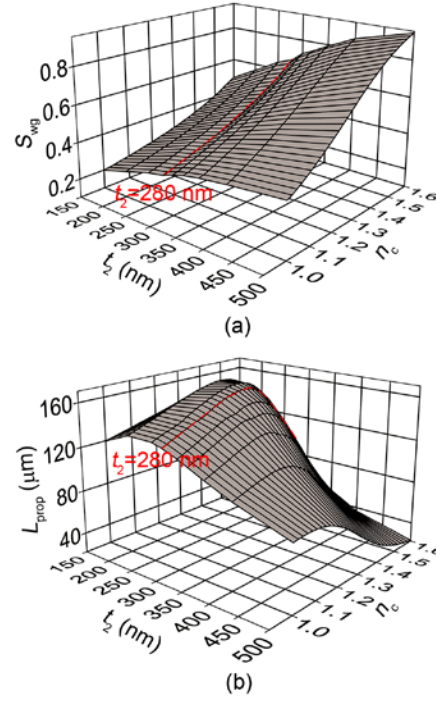


Fig. 4. (a) S_{wg} and (b) L_{prop} of the TDLSPW as functions of n_c at the wavelength of 1550 nm and $h=700$ nm.

To understand the effects of n_c on S_{wg} and L_{prop} , the distributions of electric energy density are simulated by boundary mode analysis. The x and y axes are labeled in Fig. 5(a), and the distributions of electric energy density along the y axis with different n_c are shown in Fig. 5(b). The energy in MoO_3 layer increases with the increase of the RI of analyte from 1 to 1.6, which increases the energy of evanescent field. Therefore, the interaction with the analytes detected can be enhanced. Thus, S_{wg} increases with the increase of n_c , agreeing well with the results in Fig. 4(a). However, higher n_c will induce the radiation losses, which can reduce L_{prop} , as shown in Fig. 4(b). On the contrary, the electric energy in MgF_2 layer is comparative with that in MoO_3 layer at smaller n_c . The interaction between the evanescent field and the analytes becomes weaker, which will induce the decrease of S_{wg} . Meanwhile, the ohmic losses increase due to the enhancement of the electric energy at the interface between Au and MgF_2 layers.

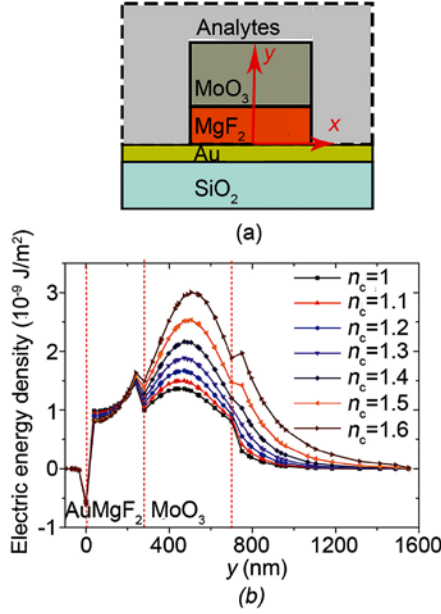


Fig. 5. (a) Cross-section profile of the TDLSPPW covered with analytes, and (b) electric energy density along the y axis ($x=0$).

B. Transmission responses

In order to fully describe the performance of the proposed sensor, the detection limit (DL) needs to be presented. For the spectral shift method, the DL characterizes the smallest RI change, which can be accurately measured and expressed as following [26]

$$DL = \frac{R_\sigma}{S} \quad (6)$$

where R_σ is the sensor resolution which describes the measurable smallest spectral shift. Q factor plays an important role in the DL of the sensor because high Q factor can reduce the spectral noise. In order to enhance the Q factor, it is crucial to reduce the losses of the resonator, especially the coupling loss [27]. Therefore, the Q factor and ER are optimized as a function of W_{gap} , as shown in Fig. 6(a). Q factor monotonically increases with the increase of W_{gap} from 100 to 500 nm. However, the ER first increases to the maximum value at $W_{\text{gap}}=320$ nm and then decreases. A larger W_{gap} can achieve higher Q factor but smaller ER , as seen from Fig. 6(a). Therefore, W_{gap} of 400 nm is chosen

for the tradeoff between Q factor and ER . In this case, the MRR is in the under-coupling state. Q factor of 541.2 and ER of 12.2 dB can be obtained. The transmission spectrum of the TDLSPPW-based MRR at W_{gap} of 400 nm is shown in Fig. 6(b). The free spectral range (FSR) of the TDLSPPW-based MRR is also shown in Fig. 6(b). Moreover, the measurement range of the wavelength shift-dependent MRR sensing is greatly limited by the FSR. The FSR of the proposed TDLSPPW-based MRR is more than 41 nm, which is beneficial to achieving larger measurement range.

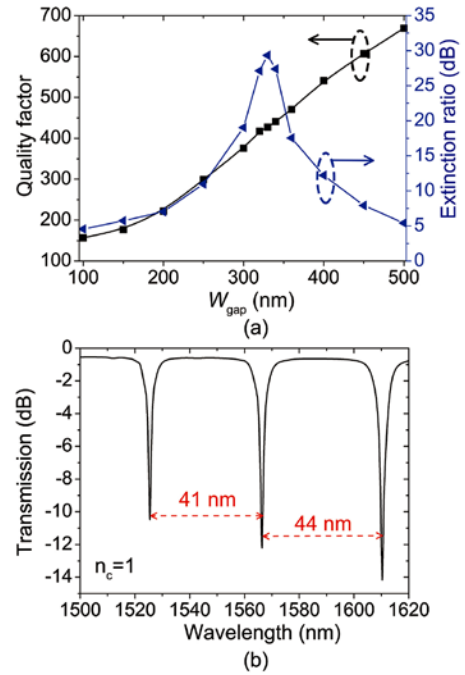


Fig. 6. (a) The dependence of Q factor and ER of the TDLSPPW-based MRR on W_{gap} at the resonance wavelength (around 1566.2 nm), and (b) transmission spectrum of the TDLSPPW-based MRR at under-coupling ($W_{\text{gap}}=400$).

C. Effect of dimensional deviations

One important practical issue of high-integrated plasmonic circuits is high sensitivity to dimensional deviations in the fabrication process. Hence, it is necessary to discuss the effects of the dimensional deviations on the performance of the TDLSPPW and TDLSPPW-based MRR to ensure the accuracy and stability of the manufactured

devices. The deviations of several structure parameters, such as w , t , t_2 , and W_{gap} , are selected to evaluate the effect on n_{eff} , L_{prop} , Q , and ER of the TDLSPW and TDLSPW-based MRR. With the optimized structural parameters t of 700 nm, w of 500 nm, t_2 of 280, and W_{gap} of 400 nm, the nominal values of $\text{Re}(n_{\text{eff}})$, L_{prop} , ER , and Q are calculated to approximately 1.361, 125.5 μm , 12.21 dB, and 541.21, respectively. The simulation results for the change of the real component of effective RI $\Delta\text{Re}(n_{\text{eff}})$ and the change of propagation length ΔL_{prop} as well as the relative deviation from the nominal values in % are presented in Figs. 7(a) and 7(b), respectively. Δw , Δt , Δt_2 , and ΔW_{gap} are the dimensional deviations.

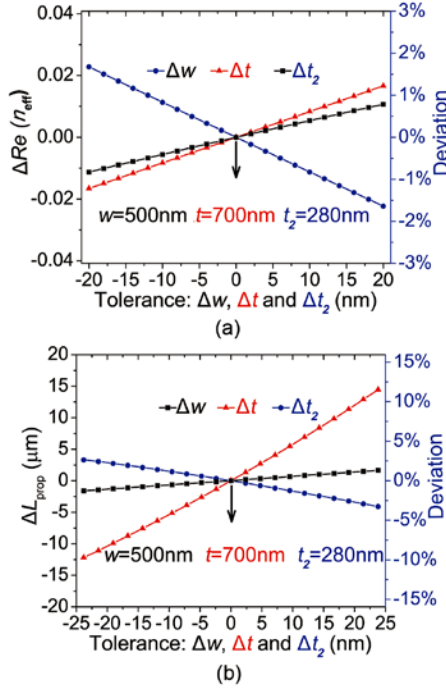


Fig. 7. (a) The $\Delta\text{Re}(n_{\text{eff}})$ and deviation from the calculated nominal value of 1.361 in %, and (b) the ΔL_{prop} and deviation from the calculated nominal value of 125.5 μm in %. Both graphs are plotted over the tolerances Δw , Δt , and Δt_2 .

As seen from Figs. 7(a) and 7(b), $\text{Re}(n_{\text{eff}})$ and L_{prop} of the TDLSPW-based MRR are very stable in regards to Δw compared to the other tolerances. The increase of Δw leads to an increase of $\text{Re}(n_{\text{eff}})$ and L_{prop} for less than 0.8 and 1.3%, respectively.

However, Δt and Δt_2 have notable influences on L_{prop} and $\text{Re}(n_{\text{eff}})$, respectively.

The deviations ΔQ and ΔER of the TDLSPW-based MRR induced by the tolerances Δw , Δt , Δt_2 , and ΔW_{gap} are also shown in Figs. 8(a) and 8(b), respectively. From Fig. 8(a), ΔQ is influenced greatly by the changes of t and W_{gap} . The effect of Δt_2 on ΔQ is less than 2.8%. Positive changes of Δw have almost no effect on the ΔQ (less than 0.83%). However, negative changes of Δw lead to a great increase of Q for a maximum of 11.8% due to the strong mode confinement in the waveguide core. It can be seen from Fig. 8(b) that the changes of Δt and Δt_2 cause a slight change of ER , and the maximum changes of ER are 0.87 and 0.33 dB, respectively. However, the Δw and ΔW_{gap} show a remarkable influence on the change of ER . For different Δw and ΔW_{gap} , the maximum changes of ER are 2.03 and 2.92 dB, respectively.

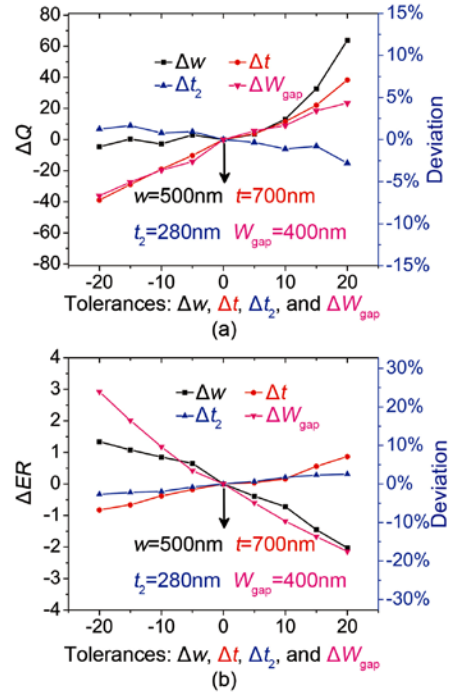


Fig. 8. (a) The ΔQ and deviation from the calculated nominal value of 541 in %, and (b) the ΔER and deviation from the calculated nominal value of 12.2 dB in %. Both graphs are plotted over the tolerances Δw , Δt , Δt_2 , and ΔW_{gap} .

From the simulation results, the Q and ER are

sensitive to w , t , and W_{gap} , but insensitive to t_2 . In order to achieve the accuracy and stability of the TDLSPW-based MRR based biochemical sensor, w , t , and W_{gap} should be optimized in the fabrication process. The simulation results for deviations in $\text{Re}(n_{\text{eff}})$, L_{prop} , Q , and ER indicate that the different tolerances could compensate each other [28].

4. Biochemical RI sensing

Detection of glucose concentration in urine is an important mean to monitor diabetes. The proposed TDLSPW-based MRR sensor can be used for biochemical detection of glucose concentration in urine since the biological molecules have larger permittivity than those of the air and water. The RI of urine is highly sensitive to the change in glucose concentration. The refractive index n_c of urine with different concentrations of glucose varies from 1.335 to 1.347 when the concentration of glucose changes from 0.015 to 10 mg/dl [29]. In order to simulate the sensing characteristics, the proposed sensor is covered by the urine with different concentrations of glucose instead of the air. The transmission characteristics of the TDLSPW-based MRR in response to n_c are shown in Fig. 9(a). The resonance wavelength of the transmission spectrum shifts toward the longer waveguide side with the increases of the RI of urine. The resonance wavelength shift as a function of n_c and its linear fit are shown in Fig. 9(b). The slope of the fitted line is 408.7 nm/RIU, which is the sensitivity of the proposed TDLSPW-based MRR sensor. The sensitivity is ~ 6 times of that obtained by the conventional Si based MRR (70 nm/RIU [30]). Following the convention of three standard deviations (3σ) of the total system noise as a measure of the sensor resolution R_σ , the RI detection limit of the proposed sensor can be calculated as following

$$DL = \frac{R_\sigma}{S} = \frac{3\sigma}{S} = \frac{0.087 \text{ nm}}{408.7 \text{ nm/RIU}} \quad (7)$$

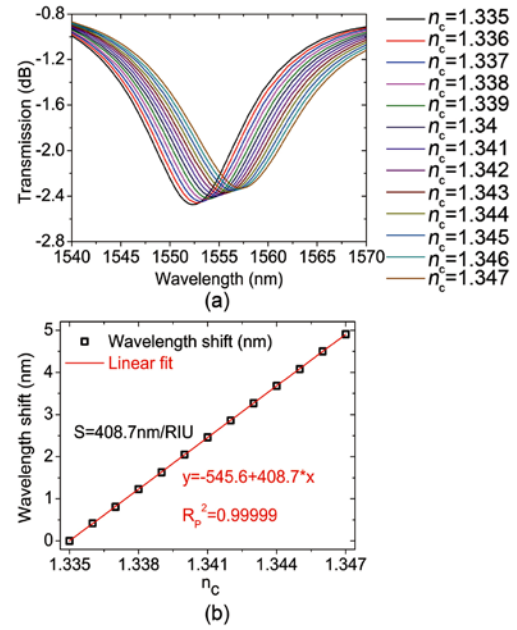


Fig. 9. (a) Transmission spectrum of the TDLSPW-based MRR with different urine RI n_c from 1.335 to 1.347 with a step of 0.001, and (b) the wavelength shift as a function of urine RI n_c .

The proposed structure can be also applied for detections of chemical gases due to the good gas-sensing property of MoO_3 thin film, such as CO , H_2 , NO_2 , and TMA (Trimethylamine) vapour sensing [31]. Here, n_c varies from 1.00 to 1.03 which includes most of the chemical gases. The transmission spectra for the different n_c are shown in Fig. 10(a). The change of the central wavelength shift with respect to the change of n_c is given in Fig. 10(b). It can be seen that the linearity between the central wavelength shift and n_c is very good, and the determination coefficient of linear fit can be up to 0.99991. S is 276.4 nm/RIU, corresponding to the slope of the fitted line. Meanwhile, the DL of 6.97×10^{-5} RIU can be also calculated by Eq. (7).

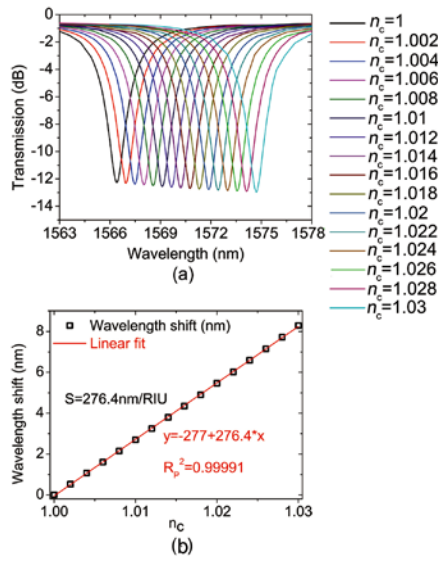


Fig. 10. (a) Transmission spectrum of the TDLSPWs MRR with different chemical gases RI (n_c) from 1.00 to 1.03 with a step of 0.002, and (b) the wavelength shift as a function of chemical gases RI (n_c).

5. Conclusions

In summary, a highly sensitive biochemical sensor made of the TDLSPW-based MRR is proposed. The propagation properties of the TDLSPWs waveguide and MRR are improved by optimizing the structure parameters. The propagation length of the proposed waveguide is $\sim 126 \mu\text{m}$, and the Q of 541.2 and ER of 12.2 dB are achieved. The effects of dimension deviations of the TDLSPW-based MRR on L_{prop} , Q , and ER have been studied. The Q and ER are sensitivity to the w , t and W_{gap} , but insensitivity to t_2 . The TDLSPW-based MRR based biochemical sensor shows the sensitivity of 408 nm/RIU and detection limit of 2.13×10^{-4} RIU for detection of glucose concentration in urine and the sensitivity of 260 nm/RIU and detection limit of 6.97×10^{-5} RIU for detection of chemical gases.

Acknowledgments

This work is supported in part by the National Natural Science Foundation of China (61307109 and 61475023), the Beijing Youth Top-notch

Talent Support Program (2015000026833ZK08), the Natural Science Foundation of Beijing (4152037), the Fund of State Key Laboratory of Information Photonics and Optical Communications (BUPT) P. R. China (IPOC2016ZT05), the Hong Kong Scholars Program 2013 (PolyU G-YZ45), key scientific and technological project of Henan province (132102210043), and Youth Scientific Funds of Henan Normal University (2011QK08 and 2012QK08).

References

1. S. A. Maier (2010) *Plasmonics-Fundamentals and Applications*. Springer Berlin 52:49-74.
2. B. Steinberger, A. Hohenau, H. Ditlbacher, and A. L. Stepanov (2006) Dielectric stripes on gold as surface plasmon waveguides. *Appl. Phys. Lett.* 88:094104.
3. T. Holmgaard, and S. I. Bozhevolnyi (2007) Theoretical analysis of dielectric-loaded surface plasmon-polariton waveguides. *Phys. Rev. B* 75:245405.
4. Z. Zhu, C. E. Garcia-Ortiz, Z. Han, I. P. Radko, and S. I. Bozhevolnyi (2013) Compact and broadband directional coupling and demultiplexing in dielectric-loaded surface plasmon polariton waveguides based on the multimode interference effect. *Appl. Phys. Lett.* 103:061108.
5. K. Hassan, F. Lerov, G. Colasdesfrancs, and J. C. Weeber (2014) Dihedron dielectric loaded surface plasmon athermal polarization converter. *Opt. Lett.* 39:697-700.
6. H. Fan, and P. Berini (2016) Bulk sensing using a long-range surface-plasmon dual-output Mach-Zehnder interferometer. *J. Lightwave Technol.* 34:2631-2638.
7. S. Papaioannou, G. Giannoulis, K. Vvrsokinos, F. Lerov, F. Zacharatos, L. Markey, J. C. Weeber, A. Dereux, S. I. Bozhevolnyi, A. Prinzen, D. Apostolopoulos, H. Avramopoulos, and N. Pleros (2015) Ultracompact and Low-Power Plasmonic MZI Switch Using Cyclomer Loading. *IEEE Photonic Tech. L.* 27:963-966.

8. [C. H. Hsieh, K. P. Lin, and K. C. Leou \(2015\) Design of a Compact High Performance Electro-Optic Plasmonic Switch. IEEE Photonic Tech. L. 27:2473-2476.](#)
9. [J. Gosciniak, and S. I. Bozhevolnyi \(2013\) Performance of thermo-optic components based on dielectric-loaded surface plasmon polariton waveguides. Scientific Reports 3:1803.](#)
10. [Y. Li, A. Ma, L. Yang, and X. Zhang \(2014\) Highly Sensitive Refractive Index Sensing with Surface Plasmon Polariton Waveguides. Plasmonics 9:71-78.](#)
11. [S. I. Bozhevolnyi, V. S. Volkov, E. Devaux, J. Y. Laluet, and T. W. Ebbesen \(2006\) "Channel plasmon subwavelength waveguide components including interferometers and ring resonators. Nature 440:508-511.](#)
12. [Y. Ma, G. Farrell, Y. Semenova, H. P. Chan, H. Zhang, and O. Wu \(2013\) Novel Dielectric-Loaded Plasmonic Waveguide for Tight-Confined Hybrid Plasmon Mode. Plasmonics 8:1259-1263.](#)
13. [O. Tsilipakos, T. V. Yioultsis, and E. E. Kriezis \(2009\) Theoretical analysis of thermally tunable microring resonator filters made of dielectric-loaded plasmonic waveguides. J Hazard Mater 106:93109.](#)
14. [H. S. Chu, Y. A. Akimov, P. Bai, and E. P. Li \(2011\) Hybrid Dielectric-Loaded Plasmonic Waveguide And Wavelength Selective Components For Efficiently Controlling Light At Subwavelength Scale. J. Opt. Soc. Am. B 28:2895-2901.](#)
15. [J. Gosciniak, V. S. Volkov, S. I. Bozhevolnyi, L. Markev, S. Massenot, and A. Dereux \(2010\) Fiber-coupled dielectric-loaded plasmonic waveguides. Opt Express 18:5314-5319.](#)
16. [P. Berini \(2009\) Long-range surface plasmon polaritons. Advances in Optics & Photonics 1:484-588.](#)
17. [R. F. Oulton, V. J. Sorger, D. A. Genov, D. F. P. Pile, and X. Zhang \(2008\) A hybrid plasmonic waveguide for subwavelength confinement and long-range propagation. Nature Photonics 2:496-500.](#)
18. [Y. Ma, G. Farrell, Y. Semenova, and O. Wu \(2014\) Hybrid nanowedge plasmonic waveguide for low loss propagation with ultra-deep-subwavelength mode confinement. Opt. Lett. 39:973-976](#)
19. [M. Y. Pan, E. H. Lin, L. Wang, and P. K. Wei \(2013\) Enhancing surface plasmon polariton propagation by two-layer dielectric-loaded waveguides on silver surface. Applied Physics A 115:93-98.](#)
20. [D. R. Lide \(2002\) CRC Handbook of Chemistry and Physics, 83rd ed. CRC Press, Boca Raton FL.](#)
21. [H. S. Chu, E. P. Li, P. Bai, and R. Hegde \(2010\) Optical performance of single-mode hybrid dielectric-loaded plasmonic waveguide-based components. Appl. Phys. Lett. 96:221103.](#)
22. [Z. Xiao-Yang, A. Hu, J. Z. Wen, Z. Tong, X. Xiao-Jun, Y. Zhou, and W. W. Dulev \(2010\) Numerical analysis of deep sub-wavelength integrated plasmonic devices based on Semiconductor-Insulator-Metal strip waveguides. Optics Express 18:18945-18959.](#)
23. [T. Yamamoto, and M. Koshiba \(1993\) Numerical analysis of curvature loss in optical waveguides by the finite-element method. J. Lightwave Technol. 11:1579-1583.](#)
24. [R. F. Oulton, G. Bartal, D. F. P. Pile, and X. Zhang \(2008\) "Confinement and propagation characteristics of subwavelength plasmonic modes. New J. Phys. 10:119-125.](#)
25. [C. Ciminelli, C. M. Campanella, F. Dell'Olio, C. E. Campanella, and M. N. Armenise \(2013\) Label-free optical resonant sensors for biochemical applications. Prog. Quant. Electron. 37:51-107.](#)
26. [IM. White and X. Fan \(2008\) On the performance quantification of resonant refractive index sensors." Optics Express 16:1020-1028](#)
27. [C. Tseng, C. Tsai, K. Lin, M. Lee, and Y. Chen \(2013\) Study of coupling loss on strongly-coupled, ultra compact microring resonators. Opt Express 21:7250-7257.](#)
28. [A. Prinzen, M. Waldow, and H. Kurz \(2013\) Fabrication tolerances of SOI based directional couplers and ring resonators. Optics Express 21:17212-17220.](#)
29. [P. Sharma, and P. Sharan \(2015\) Design of Photonic Crystal-Based Biosensor for Detection of Glucose Concentration in Urine. IEEE Sensors Journal 15:1035-1042.](#)

30. V. K. De, I. Bartolozzi, E. Schacht, P. Bienstman, and R. Baets (2007) "Silicon-on-Insulator microring resonator for sensitive and label-free biosensing. Opt Express 15:7610-7615.
31. R. Pandeeswari, and B. G. Jevaprakash (2014) Nanostructured α -MoO₃ thin film as a highly selective TMA sensor. Biosens Bioelectron 53:182-186.